Title

A sustainable sulfur–carbonaceous composite electrode toward high specific energy rechargeable cells

Journal

Materials Horizons, 7(2)

ISSN

2051-6347

Authors

Hwa, Yoon
Kim, Hyo Won
Shen, Hao
et al.

Publication Date

2020-02-10

DOI

10.1039/c9mh01224a

Peer reviewed

Sustainable Sulfur-Carbonaceous Composite Electrode Toward High Specific Energy Rechargeable Cells

Received 00th January 20xx,
Accepted 00th January 20xx

DOI: 10.1039/x0xx00000x

Yoon Hwa,[a,b,†] Hyo Won Kim,[a,b,c†] Hao Shen,[d,e] Dilworth Y. Parkinson,[d] Bryan D. McCloskey,[a,b] and Elton J. Cairns[a,b,*].

The micrometer-scale reticulated structure of highly sulfur-phillic nitrogen-doped graphene oxide (*N*rGO) that is achieved by chemically controlled nitrogen-doping degree improves chemical and electrochemical stability of the active sulfur while providing sufficient sulfur/electrolyte interface for facile electrochemical process so that high specific energy of 325 Wh/kg can be achieved.

Introduction

In recent years, the demands for high energy batteries have been growing rapidly. Within the field of electrochemical couples, the lithium/sulfur (Li/S) cell is considered to be the most promising candidate due to very high theoretical specific energy (2600 Wh/kg), the low cost and the low environmental impact of sulfur (S).[1-4] Despite its enormous potential to advance the state-of-the-art of rechargeable batteries, the actual performance of the Li/S cell was not competitive with that of Li ion cells. However, significant progress has been made in improving the performance of Li/S cells by addressing various issues associated with the S electrode.[5-19]

As a result of recent advances, researchers' attention has focused primarily on the following general practical issue: maintaining high S utilization in cells with high S mass loading and low inactive material content. In particular, an excess amount of electrolyte (i.e., generally > 10 microliters of electrolyte per milligram of S (E/S ratio = 10)) is a critical limitation for achieving high specific energy. According to the design calculation (Fig. S1), the use of a S loading of at least 6 mg/cm^2 along with a low E/S ratio (≤ 4), while maintaining good S utilization (>1000 mAh/gS) is highly desired for reaching 300 Wh/kg and more. Especially, with E/S ratio of 6 or higher, it is unable to achieve specific energy of 300 Wh/kg, even with very high S mass loading of 20 mg/cm^2. Recently, several reports have claimed to satisfy these requirements mainly by engineering the S electrode, where a carbonaceous[8-16] or aluminum (Al)[17-19] mesh (or foam) current collector was employed. However, due to technical issues associated with the manufacturing of S electrodes with foam or mesh current collectors, such as difficulty of tabbing for terminal connections (e.g. high contact impedance, brittle joint) and penetration of slurry during casting process and high implementation costs, conventional Al foil current collectors are still very desirable.

Here, we report an advanced S electrode with a conventional Al foil current collector that shows a high discharge specific capacity of 1180 mAh/gS for a high S mass loading electrode (~ 6.2 mg/cm^2) with a reduced E/S ratio of 4 without any further modifications in the cell. This achievement is attributed to the rational design of the S active material consisting of S conformally deposited and well-bound, without substantial aggregation, onto a reticulated (referring to the interconnected internal pores and channels) carbonaceous material. The reticulated structure of the S-carbonaceous composite provides a micron-scale porous structure of the S electrode that allows good accessibility of lithium ions to the active S particles and sufficient penetration of the electrolyte into the high mass loading S electrode.

Results and Discussion

To accomplish this, we successfully developed aqueous-dispersed nitrogen-doped reduced graphene oxide (*N*rGO) as a multifunctional supporting material and particularly focused on creating a reticulated architecture of the S-*N*rGO composite (S-*N*rGO) that optimizes transport of lithium ions within the S electrode. The reticulated architecture of the S-*N*rGO

[a.] *Energy Storage and Distributed Resources Division, Lawrence Berkeley National Laboratory, One Cyclotron Rd., Berkeley, California, 94720, USA*
[b.] *Department of Chemical and Biomolecular Engineering, University of California, Berkeley, California, 94720, USA*
[c.] *Department of Advanced Materials Engineering, Kangwon National University, Samcheok 25931, Republic of Korea*
[d.] *Advanced Light Source, Lawrence Berkeley National Laboratory, One Cyclotron Rd., Berkeley, California, 94720, USA*
[e.] *Center for Advancing Materials Performance from the Nanoscale (CAMP-Nano), State Key Laboratory for Mechanical Behavior of Materials, Xi'an Jiaotong University, Xi'an, Shaanxi 710049, China*
† These authors contributed equally.
Electronic Supplementary Information (ESI) available: See DOI: 10.1039/x0xx00000x

composite was successfully constructed by intentionally reducing the aggregation of all composite materials throughout the synthesis process. An aqueous *N*rGO synthetic route that simultaneously reduces the GO oxygen functional groups and introduces N functional groups enables a continuous synthetic process for conformal S deposition onto *N*rGO sheets in suspension. Existence of the N and O functional groups were demonstrated by N_{1s} X-ray photoelectron spectroscopy (XPS) and solid-state ^{13}C CP/MAS nuclear magnetic resonance spectroscopy and the results are shown in Fig. S2. By adjusting the process temperature, the physical structure of the *N*rGO sheets in the suspension was successfully controlled after the N-doping process so that more basal planes of the *N*rGO were utilized as S deposition sites during the S precipitation process. The prepared S-*N*rGO composite was collected in the form of a powder from a suspension using a lyophilization process that promotes a reticulated porous structure of the S-*N*rGO composite. A melt diffusion process followed to redistribute any S in aggregates formed during the S deposition process. (XPS of the S-*N*rGO are available in Fig. S3 and S4). This synthetic procedure provided an optimal architecture for the S-carbon composites that greatly enhanced S utilization of the high mass loading S electrodes.

Notably, conformally coated S onto the reticulated GO framework in the S-*N*rGO composite exhibited high intrinsic polysulfide absorptivity and the S-*N*rGO electrode cell delivered a (calculated) peak specific energy of 325 Wh/kg. Detailed information for the specific energy calculation is available in Table S1. This is the highest (calculated) specific energy among the Al foil-based S electrodes previously reported (see Fig. 1). Although the S electrodes noted as #6 (10.0 mgS cm^{-2}) and #7 (13.9 mgS cm^{-2}) in the Fig. 1 achieved very high S loading, they did not offer a specific energy over 300 Wh kg^{-1} due to their high E/S ratios of 13 and 15, respectively, which emphasizes importance of low E/S ratio to achieve a high specific energy.[20]

Two S-*N*rGO composites are compared in Fig. 2 (Helium ion microscopy (HIM) images) to highlight the importance of our synthesis procedures. It was demonstrated that the S-*N*rGO (synthesized using the *N*rGO prepared at 80 °C, *N*rGO) network appears to be more externally accessible and reticulated porous structure at the micron-scale and has a uniform S deposition (Fig. 2a) compared to the S-*N*rGO-100 composite (Fig. 2b) that is synthesized using aggregated *N*rGO suspension prepared at 100 °C (*N*rGO-100). At the higher temperature of 100 °C, N doping and O reduction of the GO occur more extensively, so higher N and lower O contents were obtained (Table S2), which may enhance the electronic conductivity of *N*rGO.[21] However, due to the fact that the reduction of GO (including reduction caused by the N doping) generally increases hydrophobicity of the GO sheets,[22] the *N*rGO-100 exhibited more aggregation than the *N*rGO sheets in the suspension (Fig. S5). Because of the unwanted aggregation of the *N*rGO-100 sheets, a significant portion of their basal planes, which we believe are useful to enhance specific interactions with S species, are concealed within the aggregated structure, limiting the functionality associated with the O or N functional groups. Moreover, the surface area of the *N*rGO-100 available for S deposition is also limited, which means that a thicker and less homogeneous S layer forms during the S deposition process.

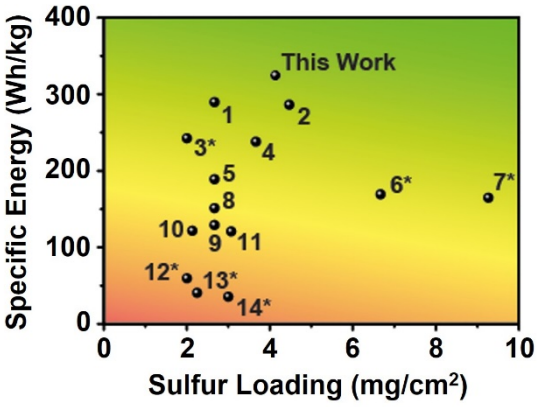

Fig. 1 Calculated peak specific energy of Li/S cells using S electrodes with a conventional aluminum foil current collector. Only the previous reports containing numerical values used for the specific energy calculation are compared in the figure (*: The cell includes an interlayer or specially-coated separator). Detailed information for the specific energy calculation, as well as the other previous reports that are not included in the figure are listed in Table S1. The numbers for the datapoints correspond to the reference numbers in the Table S1.

While the S content of both samples was approximately the same (S-*N*rGO: 85 %, S-*N*rGO-100: 84 %) as demonstrated by thermogravimetric analysis (TGA, Fig. S6 and S7), the S-*N*rGO composite exhibited a higher S vaporization temperature than that of the S-*N*rGO-100 composite. This behaviour is similar to the slightly improved thermal stability of polymer composites attributed to a homogeneously mixed nano-filler with a polymeric matrix.[23] Hence, the enhanced thermal stability could be related to the strong interaction between the conformal S layer and the *N*rGO sheets of the S-*N*rGO composite, whereas the S-*N*rGO-100 composite may contain more S that is not strongly bound by the *N*rGO sheets. Despite significantly different morphologies of the S-*N*rGO (Fig. 2a) and the S-*N*rGO-100 (Fig. 2b) composites, the isotherms of both composites follow a reversible Type Ⅱ isotherm (Fig. 2c) and slightly different Brunauer-Emmett-Teller (BET) surface area (28.5 m^2/g for the S-*N*rGO composite *vs*. 23.0 m^2/g for the S-*N*rGO-100 composite) along with a similar trend of pore size distribution (Fig. 2d), implying that similar nano-scale porous structures were formed by the lyophilization process of both composites.

Since the BET surface area analysis does not show the distinct reticulated structure of the S-*N*rGO composite, we performed three-dimensional micro X-ray computed tomography (micro X-ray CT) for the S-*N*rGO and the S-*N*rGO-100 composites. As shown in volume rendering images of the S-*N*rGO composite constructed from the 3D micro X-ray CT images (Fig. 2e), the reticulated pore structure of the S-*N*rGO composite forms continuous open channels throughout the particle, whereas the S-*N*rGO-100 composite (Fig. 2f) seems to be composed of stacked S-*N*rGO flakes with some empty spaces in between them. Based on these results, we speculate that this aggregated structure of the S-*N*rGO-100 composite restricts the Li^+ transport at high S mass loading in comparison with the more accessible and reticulated structure of the S-*N*rGO composite.

To confirm this concept, we prepared high S mass loading (~

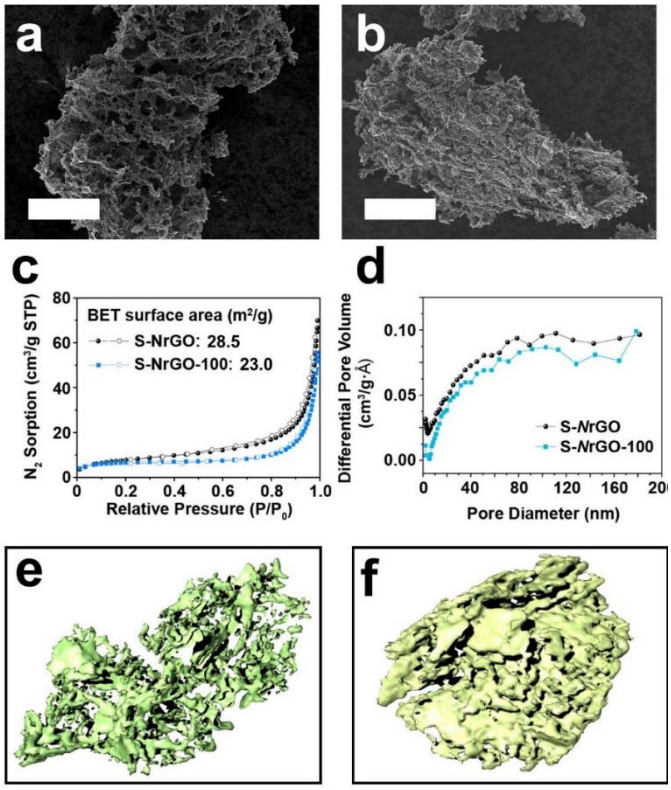

Fig. 2 Helium ion microscopy images of (a) the S-*N*rGO and (b) the S-*N*rGO-100 composite. (scale bar: 20 µm) (c) BET surface area measurement result and (d) pore size distribution of the S-*N*rGO and S-*N*rGO-100 composites. dV/dlogD data is used for differential pore volume on Y-axis. Volume rendering images of (e) the S-*N*rGO and (f) the S-*N*rGO-100 composites.

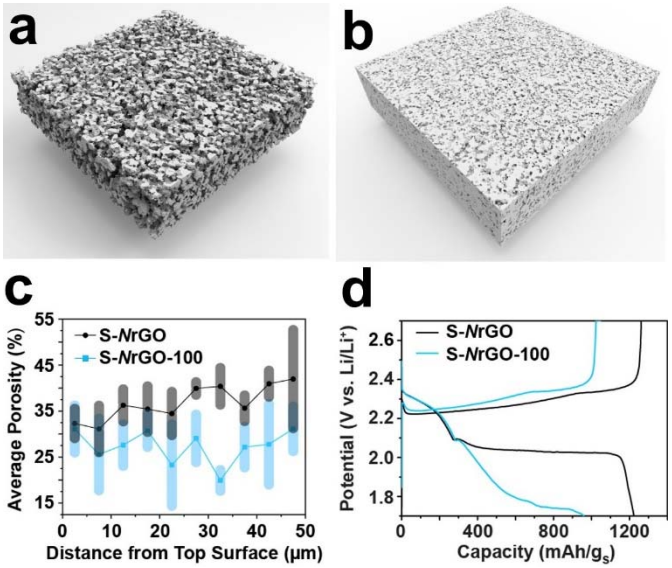

Fig. 3 Volume rendering images of (a) the S-*N*rGO electrode and (b) the S-*N*rGO-100 electrode (Scale bar: 100 µm, subvolume: 400 µm × 400 µm × 50 µm). (c) Porosity distribution of the S-*N*rGO and the S-*N*rGO-100 electrodes. (d) Voltage profiles of the S-*N*rGO and the S-*N*rGO-100 electrodes at 0.02C (1C=1675 mA/gS). The electrolyte was composed of DOL:DME (1:1, *v/v*) with 1.0 M LITFSI and 0.5 M $LiNO_3$. (S loading: ~7.2 mg/cm², E/S ratio: 5).

7.2 mgS/cm) S-*N*rGO electrodes and S-*N*rGO-100 electrodes with Al foil and elucidated the mircon-scale structure of the prepared electrodes using micro X-ray CT. Because of the reticulated structure of the S-*N*rGO composite, the S-*N*rGO electrode obviously exhibits highly porous structure as shown in the volume rendering image (Fig. 3a) and cross section image (Fig. S8a), compared to the S-*N*rGO-100 electrode (Fig. 3b and S8b). According to the average porosity estimation results (from top surface to the interior of the electrodes, Fig. 3c), the S-*N*rGO electrode exhibits significantly higher porosity with larger average pore size (Fig. S9) than the S-*N*rGO-100 electrode, where the S-*N*rGO electrode exhibited up to 50 % porosity, while the that of the S-*N*rGO-100 electrode is below 30 %.

In order to investigate the electrochemical behaviour of the S-*N*rGO and S-*N*rGO-100 electrodes, the electrodes were discharged and charged in Type 2032 coin cells (Fig. 3d) with electrochemical impedance spectroscopy (EIS) measurement being performed at the end of each process. Because of the more aggregated architecture of the S- *N*rGO-100 composite, the S-*N*rGO-100 electrode exhibited a significant discharge overpotential that caused a relatively low discharge specific capacity of 960 mAh/gS, whereas the S-*N*rGO electrode showed a specific capacity of 1220 mAh/gS with discharge plateaus around 2.30 V and 2.03 V. The Nyquist plots shown in Fig. S10 support the galvanostatic test results, where the S-*N*rGO-100 electrode exhibits larger impedance than the S-*N*rGO electrode, which is mainly due to the aggregated structure of the S-*N*rGO-100 electrode. The reticulated- structured S-*N*rGO electrode (Fig. S11a) provides sufficient channels to allow the electrolyte to penetrate the S-*N*rGO composite particles and the electrode and maintains its open structure during cell operation (Fig. S11c), while the aggregated structure of the S-*N*rGO-100 electrode (Fig. S11b) provides limited electrochemical interface due to aggregation of the active material (Fig. S11d).

To verify that our S-*N*rGO electrode is able to meet the requirements for high specific energy Li/S cells, a galvanostatic cycling test was performed for a high mass loading S-*N*rGO electrode (~ 6.2 mgS/cm²) with a low E/S ratio of 4 (~25 µL/cm² electrolyte) in a coin cell. Notably, the S-*N*rGO electrode exhibited a discharge specific capacity of ~1180 mAh/gS at 0.3 mA/cm² (Fig. 4a) and maintained a specific capacity of 700-900 mAh/gS (Fig. 4b) along with mean discharge voltage of 2.09-2.11 V for 50 cycles, which indicates significant progress in improving the specific energy (Wh/kg) of the Li/S cells. A high calculated specific energy of 325 Wh/kg was obtained, which is mainly attributed to the low E/S ratio of 4, while maintaining high S utilization (differential capacity plots are shown in Fig. S12). Long term cycling performance of the S-*N*rGO electrodes was also demonstrated with an E/S ratio of 5 (Fig. S13) and 7 (Fig. 4c) at 0.1 C, where a specific capacity of over 650 mAh/gS was maintained after 300 cycles.

Notably, the electrochemical performances of the high S loading S-*N*rGO electrodes discussed above were achieved by designing an externally accessible and reticulated structure of the active materials. However, we expect that a larger electrochemical interface between the S electrode and electrolyte raises the chance of lithium polysulfide release that causes loss of active S from the electrode. Since the S-*N*rGO electrode exhibited promising cycle life without any unique protection in the cell, it is worthwhile investigating the physical/chemical properties of the S-*N*rGO composite. To do so, we prepared S-*N*rGO composite that has almost identical

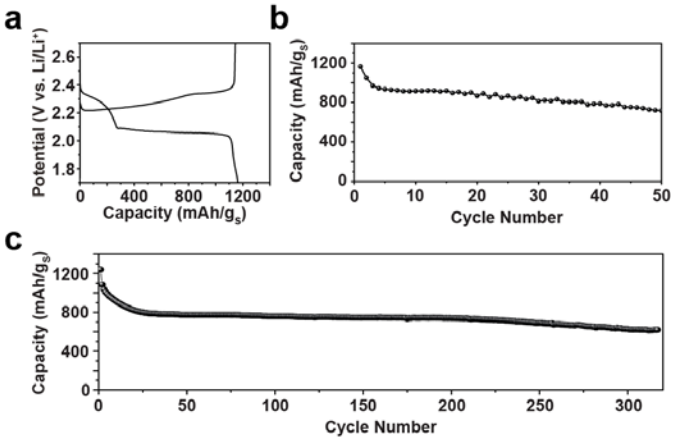

Fig. 4 Electrochemical test results of high-loading S-*N*rGO electrodes. (a) Voltage profiles and (b) cycling performances of the S-*N*rGO electrode at 0.1 C (S loading: ~ 6.2 mg/cm^2, E/S ratio: 4). (c) Cycling performance at 0.1 C and 0.05 C for discharge and charge processes, respectively (S loading: 3.0 mg/cm^2, E/S ratio: 7). The electrolyte composed of 1.0 M LiTFSI in DOL/DME (1:1, *v/v*) with 0.5 M $LiNO_3$ was used for the tests. Type 2032 coin cells were used.

chemical composition of the *N*rGO as that of the S-*N*rGO composite (XPS, Fig. S14), but has a rather undesirable aggregated S-*N*rGO microstructure, prepared by a conventional filtration process conducted to collect the S-*N*rGO composite as a powder (referred to as aggregated S-*N*rGO, HIM and SEM images shown in Fig. 5a and 5b, respectively). While the S content of both samples was 85 % as demonstrated by TGA (Fig. S15), the S-*N*rGO composite exhibited a higher vaporization temperature of the S than that of the aggregated S-*N*rGO composite, which corresponds to the phenomenon demonstrated for the S-*N*rGO and the S-*N*rGO-100 composites (Fig. S4). Since both the S-*N*rGO-100 composite and the aggregated S-*N*rGO composite form S aggregates during the melt diffusion process, it can be hypothesized that thermal stability is related to the S distribution on the *N*rGO.

The polysulfide dissolution test results also provide evidence that the S-*N*rGO composite exhibited improved retention of S compared to the aggregated S-*N*rGO composite. As shown in Fig. 5c, the test solution of the S-*N*rGO composite remained colorless after 8 hours, whereas the test solution of the aggregated S-*N*rGO composite rapidly displayed a dark yellow color, indicative of polysulfide formation due to the reaction of the S contained in the composite with the Li_2S dissolved in the test solution. The results indicate that the S in the S-*N*rGO composite dissolved into the test solution more slowly and was retained to a higher degree than the S in the aggregated S-*N*rGO composite. These results ostensibly conflict with the BET surface area analysis of each composite (Fig. S16), where the S-*N*rGO has a higher surface area and therefore likely exposes a larger S surface area to the test solution. A possible explanation of the enhanced S retention in the S-*N*rGO is an enhanced interaction between S and the non-aggregated *N*rGO, presumably due to the larger *N*rGO surface area available for interaction with S. S redistribution occurred by the thermal S infiltration process enhances binding between S and *N*rGO, possibly due to thermal new C-S bond formation on the *N*rGO carbon substructure,[24] and improved contact between S and highly S-philic N-based[25] and O-based functional groups[26] on the surface of the *N*rGO flake, while the aggregated S-*N*rGO forms aggregated S in the composite (Fig. 5b). Consequently, S-reticulated *N*rGO substrate established secures deposited S well, which enhances the thermal and chemical stability of the S in the S-*N*rGO composite. In addition, the S-philic surface of the *N*rGO can be fully utilized during cell operation, which was confirmed by chemical and electrochemical polysulfide adsorption tests (Fig. S17-S19). Li polysulfides in either the polysulfide absorption test solution and the polysulfide catholyte form Li bond with a N or O electron donor as a kind of dipole–dipole interaction, leading to secure Li polysulfide near the surface of the *N*rGO flakes.[27,28]

To demonstrate the importance of the reticulated porous structure of the S-*N*rGO composites along with chemical stability of active S on the electrochemical behaviour of the Li/S cells, galvanostatic cell tests were conducted at 0.05 C. Both the S-*N*rGO and the aggregated S-*N*rGO electrodes exhibited the typical discharge voltage profiles of a S electrode with plateaus around 2.4 V and 2.1 V (Fig. 5d). Identical first discharge plateaus that represent the formation of high-order polysulfides were demonstrated for the S-*N*rGO and the aggregated S-*N*rGO electrodes. However, a more prolonged second discharge plateau results in a higher total discharge capacity of 1410 mAh/gS for the S-*N*rGO electrode than that of the aggregated S-*N*rGO electrode (1310 mAh/gS). A similar trend was also observed during the charge process, where the S-*N*rGO electrode recovered 95.3 % of the discharge capacity after the complete charge whereas the aggregated S-*N*rGO electrode showed 90.1 % recovery of the discharge capacity. Ex-situ ultraviolet-visible (UV-Vis) spectroscopy results of the electrolytes collected from the cycled cells (Fig. 5e) confirm that a smaller amount of polysulfides remained in the electrolyte of the S-*N*rGO electrode cell after the complete discharge and charge process than the aggregated S-*N*rGO electrode cell, which illustrates the high intrinsic polysulfide absorptivity of the S-*N*rGO electrode (Absorbance peaks: 320 nm,[29-31] 350 nm,[29, 31] 420 nm[29-31] and 470 nm[29,31]). In accordance with the above results, the S-*N*rGO electrode exhibited 1.4–1.5 times higher specific discharge capacity than that of the aggregated S-*N*rGO electrode at 0.1 C and 1.0 C, which mainly resulted from the prolonged second discharge plateau (Fig. S20). EIS results at the charged state demonstrate that the reticulated structure of the S-*N*rGO significantly reduces the cell impedance associated with the electrochemical reaction rate and mass transport compared to that of the aggregated S-*N*rGO electrode (Fig. S21). As a result, the S-*N*rGO electrode exhibited significantly improved cycling performance over 300 cycles (Fig. S22).

Conclusions

In summary, we demonstrated a (calculated) peak specific energy of 325 Wh/kg for a Li/S-*N*rGO cell by the rational design of a S-*N*rGO electrode consisting of a conformal S layer deposited onto a *N*rGO framework without aggregation. The high S loading S-*N*rGO electrode (~6.2 mgS/cm^2) with a conventional Al foil exhibited a high discharge specific capacity

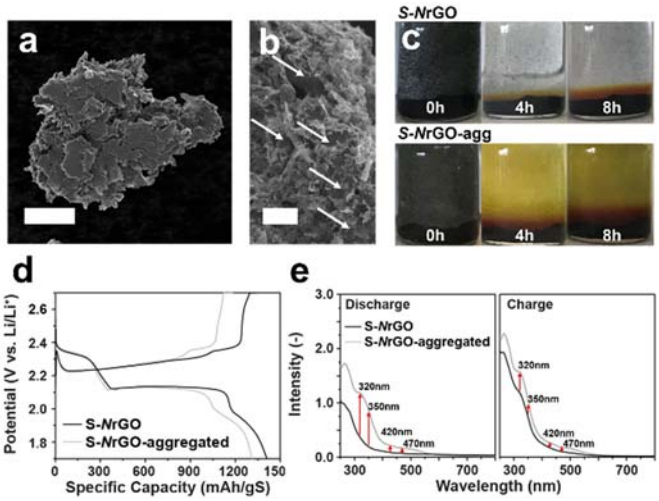

Fig. 5 (a) HIM and (b) SEM images of the aggregated S-*N*rGO composite (scale bar: (a) 20 µm, (b) 2 µm). White arrows indicate S aggregations. (c) Polysulfide dissolution test results of the S-*N*rGO and aggregated S-*N*rGO composites. The test solution is composed of 1.0 M LiTFSI and 0.5 M $LiNO_3$ in DOL/DME (1:1, *v/v*) with a stoichiometric amount of Li_2S powder added (molar ratio of 1:7 between Li_2S and S in the S-*N*rGO composite). (d) Voltage profiles of the S-*N*rGO and the aggregated S-*N*rGO electrodes at 0.05 C. The electrolyte composed of 1.0 M LiTFSI in DOL/DME (1:1, *v/v*) with 0.5 M $LiNO_3$ was used for the tests. (S loading: 1.0 mgS/cm²). (e) UV-vis test results of the electrolyte collected from the cycled cells.

of ~1180 mAh/gS at 0.3 mA/cm² with a low E/S ratio of 4, which ultimately provides one of the highest specific energy Li/S cells reported to date. It was found that this externally accessible and reticulated structure of the S-*N*rGO composite enables enhanced utilization of the highly S-philic O, N-based functional group and thermally formed C-S bonding along the *N*rGO sheet basal planes, thereby providing improved chemical and electrochemical stability of the S. In addition, the externally accessible and reticulated structure allows Li ions in the electrolyte to have good access to the inside of the *S-N*rGO composite particle and to sufficiently penetrate the electrode, while allowing dissolved polysulfides to be redeposited onto the S-*N*rGO electrode more uniformly during cell operation. This achievement improves upon the existing state-of-the-art for inexpensive and high specific energy Li/S cells, and provides critical insight into appropriate electrode microstructures and synthesis procedures for S-graphene based composites.

Conflicts of interest

There are no conflicts to declare

Acknowledgement

Work at the Molecular Foundry was supported by the Office of Science, Office of Basic Energy Sciences, of the U.S. Department of Energy under Contract No. DE-AC02-05CH11231. B.D.M. and H.W.K. gratefully acknowledge support from the National Science Foundation under grant number CBET-1604927. Micro X-ray CT (beamline 8.3.2) experiment was performed at the Advanced Light Source, which is supported by the Director, Office of Science, Office of Basic Energy Sciences, of the U.S. Department of Energy under Contract No. DE-AC02-05CH11231.

Notes and references

1 P. G. Bruce, S. A. Freunberger, L. J. Hardwick and J.-M. Tarascon, *Nat. Mater.* 2011, **11**, 19-29
2 X. Ji and L. F. Nazar, *J. Mater. Chem.* 2010, **20**, 9821-9826.
3 M.-K. Song, E. J. Cairns and Y. Zhang, *Nanoscale* 2013, **5**, 2186-2204.
4 Y. Yang, G. Zheng, and Y. Cui, *Chem. Soc. Rev.* 2013, **42**, 3018-3032.
5 X. Ji, K. T. Lee and L. F. Nazar, *Nat. Mater.* 2009, **8**, 500.
6 M.-K. Song, Y. Zhang and E. J. Cairns, *Nano Lett.* 2013, **13**, 5891-5899.
7 Y. Hwa, J. Zhao, and E. J. Cairns, *Nano Lett.* 2015, **15**, 3479-3486.
8 Q. Long, Z. Chenxi and M. Arumugam, *Adv. Energy Mater.* 2016, **6**, 1502459.
9 P. Quan, L. Xiao, K. C. Yuen, K. Joern and L. F. Nazar, *Adv. Energy Mater.* 2017, **7**, 1601630.
10 H.-J. Peng, W.-T. Xu, L. Zhu, D.-W. Wang, J.-Q. Huang, X.-B. Cheng, Z. Yuan, F. Wei, and Q. Zhang, *Adv. Funct. Mater.* 2016, **26**, 6351-6358.
11 Z. Yuan, H.-J. Peng, J.-Q. Huang, X.-Y. Liu, D.-W. Wang, X.-B. Cheng and Q. Zhang, *Adv. Funct. Mater.* 2014*,* **24**, 6105-6112.
12 Z. Li, J. T. Zhang, Y. M. Chen, J. Li and X.W. Lou, *Nat. Commun.* 2015, **6**, 8850.
13 S.-H. Chung, and A. Manthiram, *Joule* 2018, **2**, 710-724.
14 S.-H. Chung, and A. Manthiram, *Adv. Mater.* 2018, **30**, 1705951.
15 C. Wang, K. Su, W. Wan, H. Guo, H. Zhou, J. Chen, X. Zhang and Y. Huang, *J. Mater. Chem. A* 2014, **2**, 5018-5023.
16 G. Zhou, L Li, C. Ma, S. Wang, Y. Shi, N. Koratkar, W. Ren and F. Li, *Nano Energy* 2015, **11**, 356-365.
17 X.-B. Cheng, H.-J. Peng, J.-Q. Huang, L. Liu, H.-W. Zhang, W. Zhu, F. Wei and Q. Zhang, *J. Power Sources* 2014, **261**, 264-270.
18 Y. Hwa, H. K. Seo, J.-M. Yuk and E. J. Cairns, *Nano Lett.* 2017, **17**, 7086-7094.
19 J. Liu, D. G. D. Galpaya, L. Yan, M. Sun, Z. Lin, C. Yan, C. Liang and S. Zhang, *Energy Environ. Sci.* 2017, **10**, 750-755.
20 B. D. McCloskey, *J. Phys. Chem. Lett.* 2015, **6**, 4581-4588.
21 C. Mattevi, G. Eda, S. Agnoli, S. Miller, K. A. Mkhoyan, O. Celik, D. Mastrogiovanni, G. Granozzi, E. Garfunkel and M. Chhowalla, *Adv. Funct. Mater.* 2009, **19**, 2577-2583.
22 K. Erickson, R. Erni, Z. Lee, N. Alem, W. Gannett and A. Zetti, *Adv. Mater.* 2010, **22**, 4467-4472.
23 H. W. Kim, J. H. Yoon, K. M. Diederichsen, J. E. Shin, B. M. Yoo, B. D. McCloskey and H. B. Park, *Macromole. Mater. Eng.* 2017, **302**, 1700039.
24 J. Park, J. Moon, C. Kim, J. H. Kang, E. Lim, J. Park, K. J. Lee, S.-H. Yu, J.-H. Seo, J. Lee, J. Heo, N. Tanaka, S.-P. Cho, J. Pyun, J. Cabana, B. H. Hong and Y.-E. Sung, *Npg. Asia Materials* 2016**,** **8**, e272.
25 J. Song., T. Xu, M. L. Gordin, P. Zhu, D. Lv, Y.-B. Jiang, Y. Chen, Y. Duan and D. Wang, Adv. Funct. Mater. 2014, 24, 1243-1250.
26 L. Ji, M. Rao, H. Zhang, L. Zhang, Y. Li, W. Duan, J. Guo, E. J. Cairns and Y. Zhang, *J. Am. Chem. Soc.* 2011, **133,** 18522-18525.
27 T. Maihom, S. Kaewruang, N. Phattharasupakun, P. Chiochan, J. Limtrakul and M. Sawangphruk, *J. Phys. Chem. C* 2018**,** **122**, 7033-7040.
28 T.-Z. Hou, W.-T. Xu, X. Chen, H.-J. Peng, J.-Q. Huang and Q. Zhang, *Angew. Chem. Int. Ed.* 2017**,** **56**, 8178-8182.c
29 C. Barchasz, F. Molton, C. Duboc, J.-C. Lepretre, S. Patoux and F. Alloin, *Anal. Chem.* 2012, **84**, 3973-3980.
30 N. A. Cañas, D. N. Fronczek, N. Wagner, A. Latz and K. A. Friedrich, *J. Phys. Chem. C* 2014, **118,** 12106-12114.
31 Q. Zou and Y.-C. Lu, *J. Phys. Chem. Lett.* 2016, **7**, 1518-1525.